ACS APPLIED MATERIALS & INTERFACES

www.acsami.org

Research Article

Plastic Nanofluidic Sensor with a Solid-Phase Bioreactor and Dual Nanopore Reader: Studying Biological Reactions at the Single-Molecule Level

Indu A. Chandrasoma, Khurshed Akabirov, Oluwadamilola Fateru, Katie Childers, Swarnagowri Vaidyanathan, Sheila M. Barros, Maximillian Chibuike, Suresh Shivanka, Matthew Verber, Collin McKinney, Uditha Athapattu, Pubudu Premarathne, Farhad Shiri, Malgorzata A. Witek, Junseo Choi, Adam R. Hall,* Sunggook Park,* and Steven A. Soper*

Cite This: *ACS Appl. Mater. Interfaces* 2026, 18, 38600−38614

Read Online

ACCESS | Metrics & More | Article Recommendations | Supporting Information

ABSTRACT: We report a thermoplastic nanofluidic sensor (exonuclease time-of-flight; X-ToF) fabricated via nanoinjection molding that integrates an immobilized nanoscale enzymatic reactor (INER) directly with a dual in-plane nanopore ToF (DNP-ToF) reader, which not only uses the parameters typically used for resistive pulse sensing (RPS)—normalized event amplitude and time width—but the time taken for a single-molecule to travel between two pores in series. This platform enables the label-free monitoring of complex biological reactions at the single-molecule level. A critical hurdle in integrating such bioenzymatic reactions with RPS is reconciling disparate process step requirements, for example salt effects on an enzymatic reaction and high salt needs for RPS. We addressed this through strategic UV/O_3 surface engineering; an optimized 3.5 min dose created effectively charge-neutral nanopores that maximized capture rates while sustaining a robust ensemble electroosmotic flow ($5.33 \pm 0.33 \times 10^{-5}$ cm^2V^{-1} s^{-1}) and simultaneously preserving enzyme activity. To demonstrate the sensor's utility, exoribonuclease 1 (Xrn1) was used as a model. X-ToF successfully deduced the dissociation constant of an input Cas9 RNA to Xrn1 (2.4 ± 0.02 μM^{-1}) and monitored in real-time ribonucleotide generation from Cas9 with a cleavage rate of 23 nt/s. Ultimately, this platform serves as a highly versatile tool that can be repurposed for DNA, RNA, or protein sequencing simply by changing the identity of the immobilized enzyme.

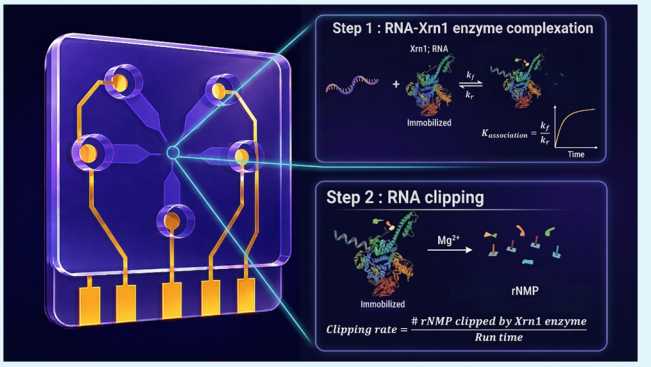

KEYWORDS: *resistive pulse sensing, solid-phase enzymatic reactions, single-molecule detection, nanofluidics, plastic nanoinjection molding*

INTRODUCTION

Over the last few decades researchers have used RPS for a number of compelling applications, such as determining the primary structure of biopolymers such as DNA, RNA, and proteins. Typically, RPS uses either a biological[1] or solid-state[2,3] nanopore embedded within a free-standing membrane (i.e., out-of-plane pores). However, protein nanopores have low tolerances under harsh mechanical and chemical conditions, and while solid-state nanopores can address those concerns, they are challenged by fabrication costs and generating high-throughput devices comprised of many pores.[4]

Recently, we reported the use of in-plane thermoplastic nanopores for RPS that addresses many of the challenges associated with out-of-plane pores such as the ability to manufacture the pores with unique architectures via high throughput manufacturing methods such as nanoimprint lithography or nanoinjection molding and arrange the pores into different configurations to allow implementation of unique readout formats with new data types not readily available using out-of-plane pores.[4−7] Another advantage of thermoplastics is that they can be irradiated with UV/O_3 to activate their surfaces that alters the surface wettability by generating surface-confined functional groups.[8−10] In addition, the degree of surface charge can be controlled by dosing the plastic with different levels of UV/O_3 radiation.[11]

In this work, we report a novel nanosensor coined an exonuclease time-of-flight (X-ToF) sensor, made from a plastic via nanoinjection molding. The unique aspect of this sensor is

Received: April 28, 2026
Revised: June 17, 2026
Accepted: June 22, 2026
Published: June 29, 2026

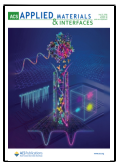

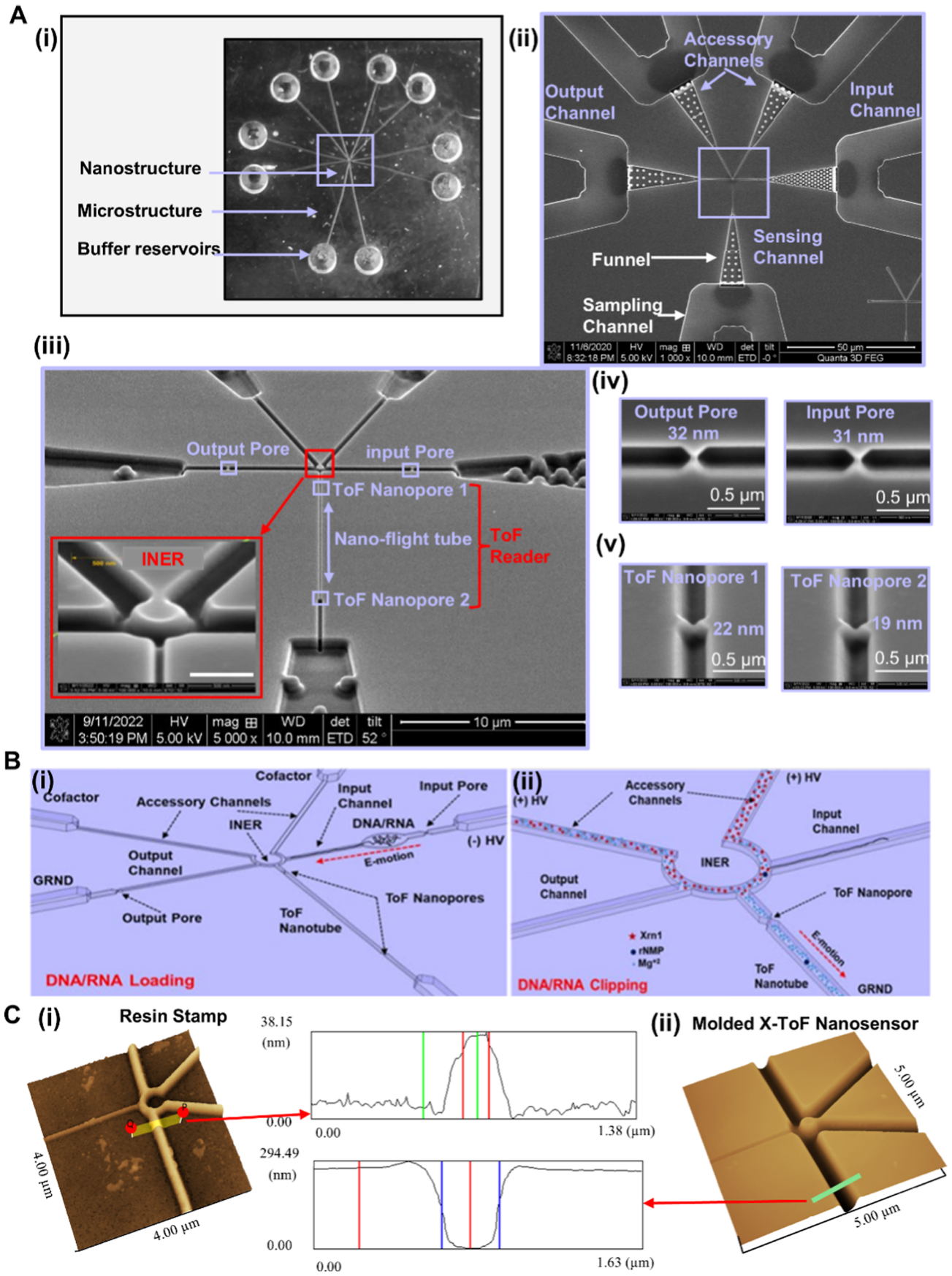

Figure 1. X-ToF sensor for processing single molecules. (A) Layout of components: (i) integrated device with its reservoirs; (ii–v) SEM images of the micro/nanofluidic network and in-plane nanopores derived from a Si master that was fabricated using photolithography and FIB milling. (B) Operational schematics showing: (i) electrokinetic biopolymer loading; and (ii) enzymatic cleavage of a single RNA molecule within the INER

https://doi.org/10.1021/acsami.6c08660
ACS Appl. Mater. Interfaces 2026, 18, 38600−38614

Figure 1. continued

using an immobilized Xrn1 and Mg^{2+} cofactor. (C) AFM images and cross sections of: (i) the resin stamp made via UV-NIL; and (ii) the final nanoinjection molded device make in COP.

that it consists of an immobilized nanoscale enzymatic reactor (INER) coupled directly to a dual in-plane ToF nanopore (dToF) reader, which could be used to identify the products of the INER in real time using RPS at the single-molecule level. The nanofluidic network engineered into the sensor could load single biopolymers and deduce whether the input associated or not with a surface immobilized enzyme in the INER by monitoring the presence/absence of RPS signals generated by input/output nanopores; these pores also assured that a single molecule was resident within the INER. The X-ToF sensor could also monitor INER products in real time using the dToF reader. While standard RPS primarily provides peak amplitude and dwell time as single molecule identifiers, the dToF reader featured a micrometer-scale flight tube placed between two in-plane pores. This unique architecture allowed the measurement of a molecule's ToF, which is determined by its apparent electrophoretic mobility and specific interactions with the flight tube walls adding an additional dimension for high-accuracy identification of single molecule in a label-free manner.

Because of the coupling two functional elements within the X-ToF sensor, bioenzymatic reactions could be monitored in real-time. As an example of this capability, we present data on using X-ToF for deciphering the complex dynamics of a processive exoribonuclease I (Xrn1) acting on an RNA substrate. Xrn1 plays a critical role in regulating mRNA turnover, gene expression, and defending against viral infections.[12] Xrn1 degrades RNAs in a 5′ → 3′ direction by removing one rNMP from an RNA substrate in the presence of Mg^{2+}. According to the literature, Xrn1 can degrade >10.5 kb of RNA processively when surface immobilized.[11] Using X-ToF, we will show that we can elucidate the thermodynamic and kinetic characteristics of Xrn1 at the single-molecule level. To our knowledge, no tool has been reported that enables label-free investigation of the complex dynamics of exonucleases while also allowing discrete monitoring of the two-reaction steps associated with a processive exonuclease at the single-nucleotide level.

RESULTS AND DISCUSSION

X-ToF Nanopore Sensor: Architectural Layout and Operation

The X-ToF sensor is a thermoplastic nanofluidic device fabricated from cyclic olefin polymer (COP; see Figure S1 for description of the fabrication steps) with a cyclic olefin copolymer (COC) cover plate and designed to allow the input of single molecule substrates into the INER and monitor their reaction products in real time. The devices were fabricated via nanoinjection molding from resin stamps. This optimized molding and thermal fusion bonding process yields a highly reliable fabrication success rate of >90%, achieving high replication fidelity with an interdevice relative standard deviation of <5% for structures <20 nm.[13]

As shown in Figure 1A(i), the platform's layout consisted of ten buffer reservoirs for reagent introduction, a microchannel network, and a central nanostructure hub. The fluidic architecture featured five distinct channels converging at the center: two accessory microchannels, an input channel, an output channel, and a Time-of-Flight (ToF) channel (Figure 1A(ii)). Each of these channels was separately connected to a tapered funnel that served a dual purpose: (i) acts as a physical filter to prevent macromolecular clogging; and (ii) significantly lowers the entropic barrier for target biopolymers entering the pore generating high loading efficiency (see Figures S2A − target loading − and S2B − enzymatic cleavage and product identification).[14] Specifically, the accessory channels allowed for the introduction of enzymes for surface immobilization into the INER and delivery of cofactors, such as Mg^{2+}, to initiate bioenzymatic reactions. The input and output channels were used to transport single molecules into the INER, while the ToF channel was used to identify enzymatic products. These channels were further connected to the core processing units: INER and the dToF reader (Figure 1A(iii)).

The INER was designed to allow for the immobilization of enzymes,[11,15] such as Xrn1, and was designed to allow for the site-specific surface immobilization of the enzyme within the INER. Flanking the INER were a pair of in-plane input and output nanopores (Figure 1A(iv)) with dimensions of ∼30 nm in width and depth. These pores enabled the determination of the association constant (K_{assoc}) by distinguishing between paired RPS events (unbound substrate) and single events (enzyme-associated complex). The input pore also assured that a single molecule was loaded into the INER. The second major component was the dToF reader (Figure 1A(iii)), which featured a 10 μm long nanoflight tube (50 × 50 nm) situated between two in-plane nanopores (Figure 1A(v)) typically <20 nm, but were reduced to <10 nm in apparent diameter following thermal fusion bonding a COC cover plate to the COP substrate. The nanopore scaling was optimized to detect intact RNAs and detect/identify single rNMPs released during the enzymatic reaction using the dToF reader. The integration of these units into a single chip allowed for single-molecule processing followed by real-time product identification.

The X-ToF operational workflow involved two main steps: (i) a single biopolymer (RNA or DNA) was electrokinetically loaded into the INER by applying a voltage across the input and output channels while the accessory and sensing channels remained floating (Figure 1B(i)). (ii) After isolating a single RNA molecule (Figure 1B(ii)), the reaction was initiated by introducing a cofactor (Mg^{2+} in this example), through the accessory channels electrokinetically. This was achieved by applying a voltage across the INER and the dToF reader while the input and output channels were floated allowing cleavage products to be identified in real-time as they traveled through the dToF. It is important to note that single-molecule routing through this complex fluidic network does not rely on physical valves. Instead, it is governed entirely by selective electrokinetic control to actively steer analytes.

There were three basic steps for the fabrication process, which involved generation of a Si master via optical lithography (microstructures) and focused ion beam milling (nanostructures). (ii) Generation of a resin stamp that served as the mold insert for replication of the finished part, which involved using UV-nanoimprint lithography (see Figure 1C(i) for SEM of this insert). (iii) Generation of the final plastic part

https://doi.org/10.1021/acsami.6c08660
ACS Appl. Mater. Interfaces 2026, 18, 38600−38614

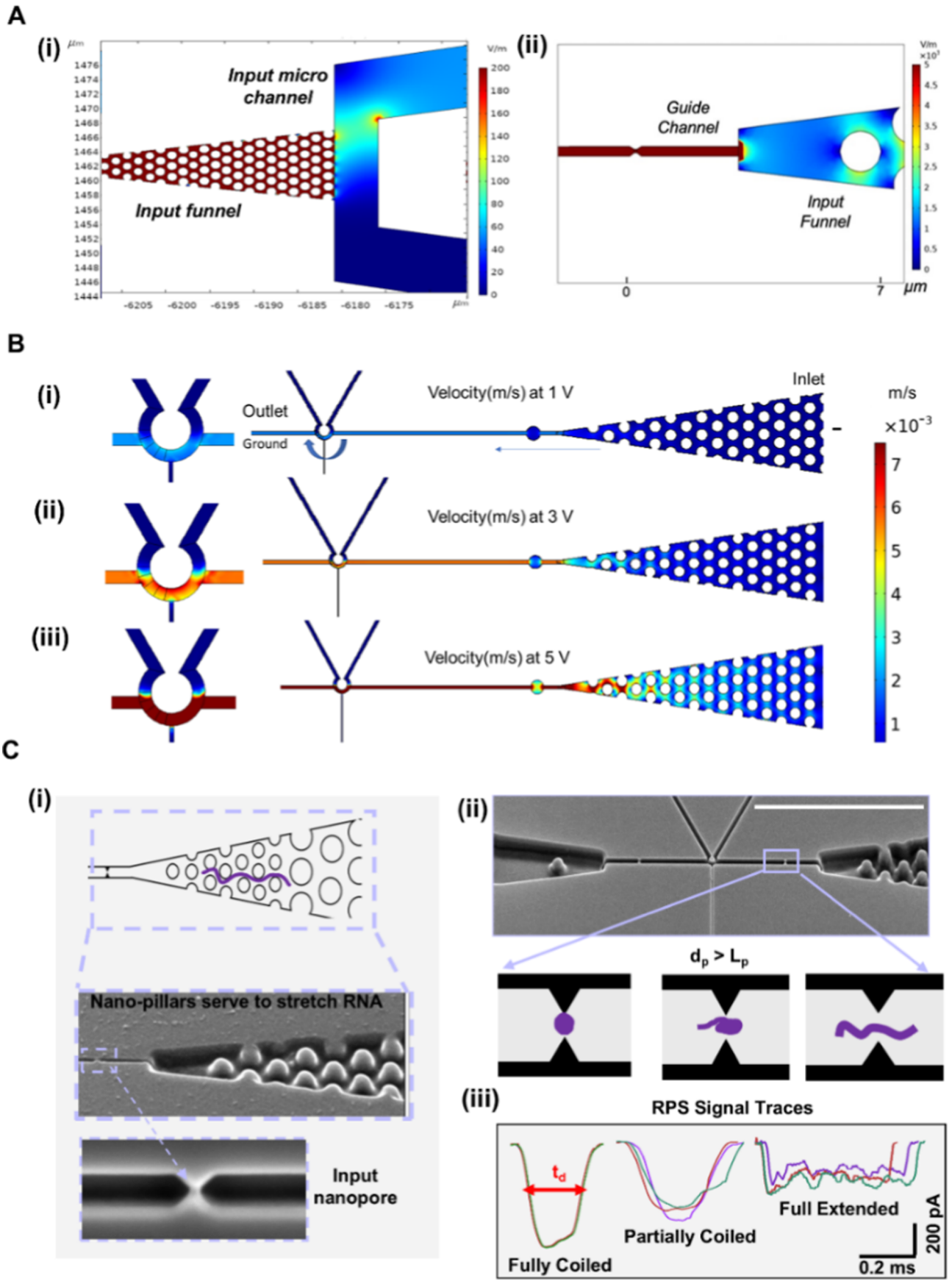

Figure 2. Loading of single biopolymers into the X-ToF sensor. (A) COMSOL simulated electric field distribution in the sampling input funnel and microchannel (i) and the input channel with its accompanying in-plane nanopore (ii). (B) Fluidic electrokinetic velocity profile at 1 (i), 3 (ii), and 5 (iii) V demonstrating electrokinetic control for the loading process of single molecules across the input/output channels and INER. In this

https://doi.org/10.1021/acsami.6c08660
ACS Appl. Mater. Interfaces 2026, 18, 38600−38614

Figure 2. continued

case, the accessory channels and dToF channel are floated. (C) Structural and signal analysis: (i) SEM/schematic of the pillar-arrayed funnel for RNA transport (persistence length = 6−9 nm); (ii) SEM of the in-plane pores flanking the INER; (iii) RPS traces for Cas9 RNA translocation distinguishing between fully coiled, partially coiled, and fully extended configurations based on dwell time differences. There are three different RPS traces shown for each configuration across the input pore.

using nanoinjection molding (see Figure 1C(ii) for SEM of the COP molded part).

Loading Single Molecules into the X-ToF Sensor

We evaluated the performance of the X-ToF sensor using Xrn1 action on a Cas9 RNA substrate (4512 nt). The loading of the target RNA into the sensor was achieved electrokinetically by applying a voltage across the input/output channels and the INER as described in Figure S2A(i). Schematics showing extensive layouts of the input/output fluidic network with the INER are shown in Figure S2A(ii) and an SEM of this network in Figure S2A(iii). The equivalent electrical circuit is shown in Figure S2A(iv). To facilitate capture of biopolymers, the input channel incorporated a 3D-tapered region containing a pillar array. These structures are critical for lowering the entropic barrier for single molecule entry into the sensor and improving the loading efficiency from a microscale channel by extending the electric field into the microsampling channel.[16]

COMSOL simulations were conducted to map the electric field distribution during the RNA loading phase during which the accessory channels and flight tube were allowed to float to maintain field focus (Figure S2A(v)). Despite the complexity of this fluidic network, there was still sufficient electric fields displayed within the in-plane nanopores (see Figure S2A(vi)), we could still observe sufficient signal-to-noise ratios to see current transients elicited by single molecules as will be shown in subsequent sections of this manuscript.

As illustrated in Figure 2A(i), the inclusion of specific fluidic elements allowed the electric field to extend significantly from the input funnel into the sampling microchannel, ensuring high loading efficiency from the sampling microchannel. Figure 2A(ii) further highlights the high electric field generated at the junction of the 250 nm × 250 nm input channel and the tapered funnel. This design avoided inefficiencies of blunt interfaces, which provide poor sampling efficiency.[14] Strategic operational considerations, such as applying a cathodic voltage at each reservoir flanking the input channel, can further enhance loading efficiency of anionic species as well as the low electroosmotic flow (EOF) elicited by thermoplastic substrates with nanoscale channels.[3,17] These design considerations allowed the X-ToF sensor to load and detect as little as 4 fg of input material.

Figure 2B(i−iii) shows that as the voltage is increased from 1 to 5 V, the electric field remained primarily restricted within the loading network. This allowed for precise control of fluidic motion, preventing the input molecule from leaking into the accessory channels or the dToF reader during loading. If diffusional leaking does occur, a blocking voltage could be applied to generate a counteracting EOF.

The physical architecture of this loading system is visible in the SEM images of Figure 2C(i),(ii), which show the input funnel, pillar arrays, and the ∼30 nm input pore. Because the apparent pore diameter (d_p) is significantly larger than the persistence length (Lp) of the RNA (6−9 nm),[18] the molecule can adopt various shapes during entry. The resulting RPS traces in Figure 2C iii confirmed this as the dwell time (t_d) revealed three distinct translocation dynamics: randomly coiled, partially coiled, and fully extended RNA. Collectively, these results validate the sensor's ability to achieve high loading efficiencies required for single-molecule analysis. With the target successfully loaded, the next challenge was reconciling the disparate ionic environments required for bioenzymatic catalysis and high-fidelity RPS detection.

Following loading of a single substrate molecule into the INER and its association to a processive enzyme, the reaction could be initiated by introducing a Mg^{2+} cofactor into the INER with online shuttling the reaction products into the dToF reader for detection and identification. Figure S2B(i) shows the applied voltage layout for this phase of X-ToF operation with an SEM of the dToF reader interfaced to the INER in Figure S2B(ii). The equivalent circuit for the dToF reader is shown in Figure S2B(iii) with a COMSOL simulation showing the electric field distribution in Figure S2B(iv); clearly shown in the inset is the high electric field within the in-plane nanopore that would facilitate RPS of even a single ribonucleotides.[14]

Balancing Salt Effects and Surface Charge for the X-ToF Sensor for Coupled Enzymatic/RPS Operation

Integrating the X-ToF sensor's INER with its dToF reader required navigating the disparate ionic conditions required for optimized catalytic activity (Xrn1 in this case) and RPS. While high salt concentrations typically optimize RPS signal-to-noise ratios,[19] processive exonucleases exhibit decreased efficiency under high salt conditions.[20,21] To address this conflict, we systematically investigated the interplay between salt concentration, surface charge, and enzyme performance to establish optimal conditions for the INER/dToF reader integration.

We first evaluated the impact of salt on the digestion efficiency of processive exonucleases, including λ-Exo, Xrn1, and PNPase, using an immobilized microscale enzymatic reactor (IMER) to establish a baseline for scaling effects (Figure S3). As can be seen in Figure 3A, our results demonstrate that surface immobilization enhanced enzyme activity across a broad range of salt concentrations compared to solution-phase reactions. This increased activity is likely attributed to the local electrostatic environment within the electrical double layer (EDL). At KCl concentrations between 200 and 1000 mM, the Debye length (λ_D) is approximately 0.9−1.2 nm. Atomic force microscopy (AFM) data suggested that the immobilized enzyme resides primarily within the diffuse layer, where the ion distribution remains distinct from the bulk solution. Despite this stability, maintaining peak enzymatic efficiency required salt concentrations <250 mM, which can complicate standard RPS detection.

To maintain high RPS capture rates at these lower salt concentrations, we engineered the thermoplastic surfaces of X-ToF using controlled UV/O_3 dosing to modulate surface charge density. Dosing from 0 − 15 min produced a stepwise reduction in the water contact angle as well as increases in the presence of a carbonyl band in the ATR-FTIR spectrum and fortified through XPS data (see Figure S4A−D). We found

https://doi.org/10.1021/acsami.6c08660
ACS Appl. Mater. Interfaces 2026, 18, 38600−38614

A

Enzyme	Enzymatic reaction type	Efficiency of Digestion (%) in Different Salt Concentrations					
		0 M KCl	0.125 M KCl	0.250 M KCl	0.500 M KCl	0.750 M KCl	1.00 M KCl
Lambda exonuclease	In Solution	90.0 ±3.9	26.0 ±4.3	21.0 ±3.6	23.0 ±4.4	-	3.0 ±3.1
	Solid Phase	90.7 ±3.0	76.9 ±3.4	67.5 ±3.3	66.0 ±12.6	-	48.4 ±16.9
Exoribonuclease I	In Solution	91.0 ±5.1	-	71.0 ±3.0	57.0 ±4.5	42.0 ±1.2	12.0 ±1.3
Polynucleotide phosphorylase	In Solution	93.0 ±3.2	-	56.0 ±5.6	51.0 ±1.3	39.0 ±2.1	15.0 ±3.4

B

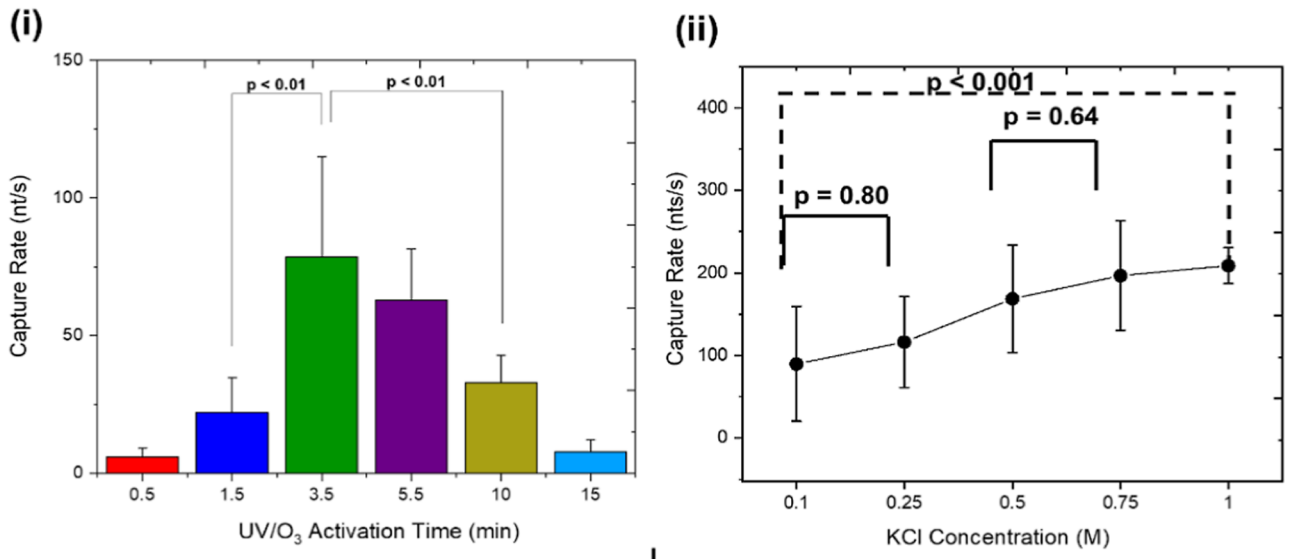

C

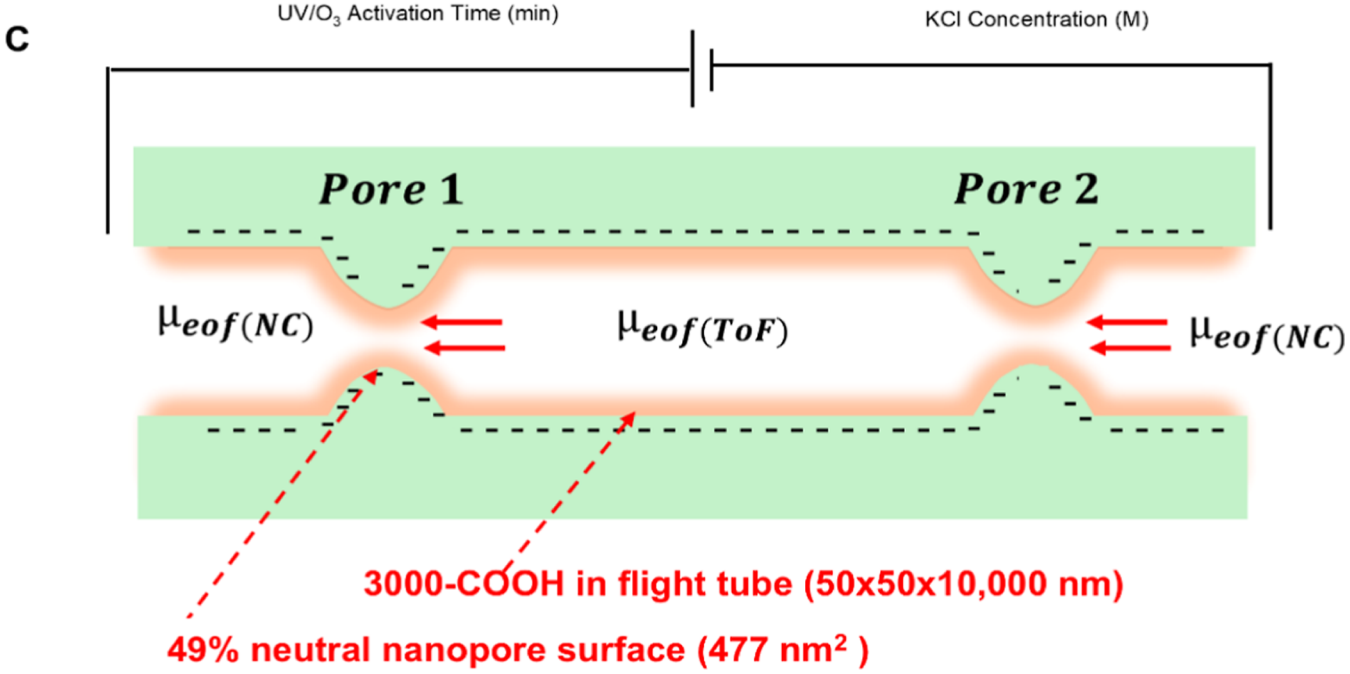

Figure 3. Optimization of surface charge and salt concentration for X-ToF. (A) Comparative digestion efficiency of processive exonucleases (λ-Exo, Xrn1, and PNPase) for in-solution versus solid-phase (IMER) digestions across varying KCl concentrations. (B) Nucleotide capture rate optimization: (i) As a function of UV/O_3 activation time at a constant KCl concentration of 100 mM; and (ii) vs KCl concentration for a 3.5 min UV/O_3 dose. (C) Schematic of the dToF reader with its different sizes, charge distribution, and EOFs. Poisson analysis indicated predominately

https://doi.org/10.1021/acsami.6c08660
ACS Appl. Mater. Interfaces 2026, 18, 38600−38614

Figure 3. continued

surface charge-neutral in-plane pores (~0.7 groups) and charged 10 μm length flight tube (~3000 groups) sustaining an ensembled EOF throughout the fluidic network. Surface charge arises from deprotonation of −COOH groups generated by photooxidation of COP and COC using UV/O_3 irradiation.

that a 3.5 min activation time provided the ideal balance for the sensor's operation. Specifically, a 3.5 min UV/O_3 dose combined with 100 mM KCl resulted in a maximum capture rate for deoxyadenosine monophosphate (dAMP), representing a >200% improvement over other activation times as seen in Figure 3B(i). Furthermore, as shown in Figure 3B(ii), for a 3.5 min activation the capture rate was only weakly dependent on salt concentrations below 750 mM. Lower doses maintained linear I−V characteristics for the dToF reader nanopores, whereas higher doses (e.g., 10 min) generated nonlinear I−V curves indicative of ion current rectification (ICR) caused by asymmetric salt profiles (Figure S4E). COMSOL simulations indicated higher salt gradients within the nanoflight tube (see Figure S4F,G).

Local heterogeneity within the device was further revealed through super-resolution (STORM) microscopy and XPS analysis, which confirmed that a 3.5 min dose produces a surface carboxyl density of approximately 0.0028 nm^{-2} (Figure S5A−C).[10] As seen in Figure 3C showing the relative sizes of the in-plane pores and the flight tube, Poisson analysis of these surface groups within the small in-plane pores (477 nm^2 surface area) indicated that ~49% of the pores were effectively charge-neutral, while the intervening 10 μm nanoflight tubes were highly negatively charged with ~3000 carboxyl groups. This heterogeneity allowed the nanopores to operate with minimal local EDL interference while the flight tube sustained a robust ensemble EOF of $5.33 \pm 0.33 \times 10^{-5}$ cm^2V^{-1} s^{-1} (see Figure S5D). This balanced environment ensures that single-molecule reaction products can be effectively shuttled into and identified by the dToF reader for lower surface activation conditions (≤3.5 min activation time).

Site-Specific Enzyme Immobilization within the INER

The site-specific immobilization of Xrn1 within the INER was achieved by leveraging the structural asymmetry of the enzyme in coordination with precise fluid manipulation using the extensive fluidic network of X-ToF and electrokinetic operation. Xrn1 possesses 45 surface-exposed lysine residues; however, its primary structure reveals that only approximately four of these residues are located near the catalytic site, while the majority are positioned on distal surfaces (Figure S6). This natural distribution is critical for maintaining enzymatic activity once immobilized as it favors an orientation that keeps the active site accessible to solution-borne RNA substrates rather than masking it against the INER surface.

To facilitate covalent attachment, we utilized EDC/NHS coupling chemistry to link the primary amines of the lysine residues to the surface-confined carboxylic acid (−COOH) groups generated via UV/O_3 activation of the COP substrate and COC cover plate as seen in Figure 4A. We specifically employed a low UV/O_3 dose (18.0 mW/cm^2 for 3.5 min) to maintain a sparse −COOH density, a strategy designed to prevent multisite attachment, which can lead to protein denaturation and also require the need for minimal salt requirements for optimal RPS performance (Figure S6). Site-specific immobilization of the enzyme within the INER was accomplished by applying a voltage to the accessory channels and across the INER.

To validate the spatial precision of this loading process as seen in Figure 4B, we utilized a dye-labeled oligonucleotide reporter containing a 5′ primary amine. Figure 4B(i) shows the absence of a fluorescent signal in the buffer only X-ToF sensor. After introducing the dye-labeled oligonucleotide reporter, fluorescence was visible. After washing the INER, fluorescence imaging (Figure 4B(ii)) confirmed that immobilization was confined within the INER and the associated accessory microchannels used for reagent introduction. Notably, no fluorescence was detected within the nanoflight tube demonstrating that our loading protocol prevented enzyme deposition in the downstream sensing region (see Figure 4B(ii)). While enzyme was present in the accessory channels, COMSOL simulations verified that during enzyme loading, reagent flow was restricted to the INER and not the input/output channels (Figure 4C (i)-(iii)). However, under electrokinetic control during RNA loading, the RNA substrate was effectively excluded from entering the accessory channels, which remain floating during the loading phase, ensuring that the enzymatic reaction occurred within the central reactor junction close to the dToF reader to ensure efficient loading of reaction products into the flight tube where they can be detected and identified.

The functional activity of the immobilized Xrn1 within the INER was first evaluated by monitoring the digestion of a single Cas9 RNA molecule (4512 nt) stained with SYTO 82. The enzymatic reaction was dependent on the presence of the Mg^{2+} cofactor; upon introduction of the cofactor, we observed a progressive loss of fluorescence intensity as a function of time (Figure 4D (i)), which arose from the sequential loss of rNMPs from the Cas9 molecule. In Figure 4D (ii), a graph of relative intensity vs time shows the background (blue), the fluorescence signal with the cofactor (green), and the fluorescence signal without the cofactor (red). By quantifying this decay, we calculated a provisional clipping rate (k_{clip}) of approximately 25 nt/s, which was determined by the time taken for the fluorescence to decay to the background level (180 s) and the total length of the Cas9 RNA molecule (4512 nt). This kinetic value is in excellent agreement with results obtained from microscale solid-phase reactions in an IMER,[11] indicating that the transition to a nanoscale reactor does not impose mass-transfer limitations or alter the fundamental activity of the enzyme. This successful demonstration of site-specific immobilization and real-time, solid-phase digestion sets the stage for the sequential identification of the association and clipping steps of the enzyme using enzyme−substrate binding and subsequent mononucleotide detection using the downstream dToF reader.

X-ToF Sensor for Determining Salt Effects on K_D of Xrn1

During RNA loading and electrokinetic shuttling into the INER, we found that the RNA moved from cathode-to-anode and thus against the X-ToF sensor's EOF (Figure 5A(i)). Those RNAs loaded can complex with surface immobilized Xrn1 within the INER or not. This complexation is reversible

https://doi.org/10.1021/acsami.6c08660
ACS Appl. Mater. Interfaces 2026, 18, 38600−38614

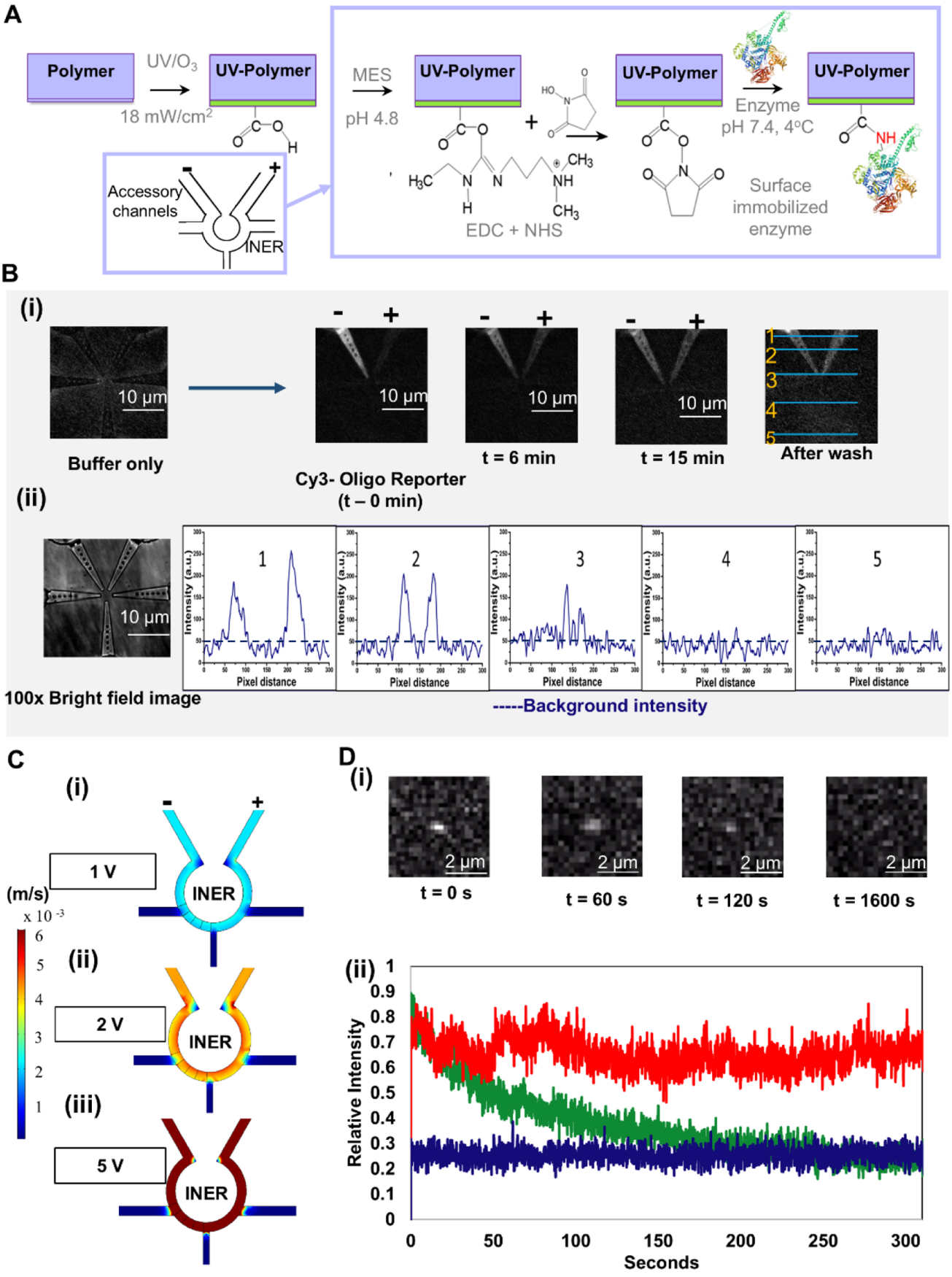

Figure 4. Site-specific enzyme (Xrn1) immobilization and fluorescence-monitored digestion in INER. (A) Schematic of UV/O_3 surface activation to generate−COOH groups for covalent coupling to the enzyme via EDC/NHS coupling chemistry. (B) (i) Fluorescence images of Cy3-labeled reporter loading as a function of location within the INER/dToF interface; and (ii) intensity profiles confirming enzyme localization within the

https://doi.org/10.1021/acsami.6c08660
ACS Appl. Mater. Interfaces 2026, 18, 38600−38614

Figure 4. continued

INER. The numbers in the fluorescence images in (ii) refer to the numbered locations within the INER shown in (i). (C) COMSOL simulations (1, 2, 5 V for (i−iii), respectively) validating electrokinetic flow around the INER pillar. (D) INER digestion of a single Cas9 RNA molecule. (i) Time-stamped images showing fluorescence loss during single Syto82-labeled Cas9 RNA. The bright spot represents the single RNA molecule. (ii) Intensity plots for background (blue), active digestion with Mg^{2+} (green), and control without cofactor (red) Cas9 digestion.

and $K_{association}$ can be determined as shown in Figure 5A(ii); K_D is simply equal to $1/K_{association}$. Because the input and output channels contained in-plane nanopores (Figure 5B(i)), we used RPS to determine the presence of paired versus unpaired RPS events. Paired events indicated no association between the RNA and the surface immobilized Xrn1 while unpaired events indicated a successful association event (Figure 5B(ii)).

To determine how the salt concentration affected RNA-enzyme complexation, we examined K_D of Xrn1 in three different KCl concentrations. Figure 5C (i−iii) shows RPS traces for input Cas9 RNA into the INER. In the RPS current traces, the blue stars represent unpaired events indicating RNA complexation with the immobilized enzyme, and red/green stars represent paired events (red star represents the first event of the pair, and the green star represents the second event of the same paired event) and thus, no Xrn1/Cas9 RNA association. Over the duration of these experiments, we registered >100 RPS events and measured the percentage of paired events, which was 70 ± 10% for 1 M KCl, 47 ± 7.5% for 0.5 M KCl, and 27 ± 5.3% for 0.1 M KCl. As can be seen in Figure 5C(iv), RPS data yielded K_D values (μM^{-1}) of 12.6 ± 1.6, 6.2 ± 0.4, and 2.4 ± 0.02, respectively. High salt concentrations can hinder the binding of the enzyme to its substrate by shielding charges on both the enzyme and substrate reducing electrostatic interactions between them.[22] For example, Longley and Mosbaugh investigated the activity of a 3′ → 5′ exonuclease in different salt concentrations (KCl and NaCl),[20] and found that the enzyme exhibited maximal activity at a salt concentration of 0.15−0.20 M;[20] these observations are consistent with our X-ToF results. However, in the aforementioned reference a composite of association efficiency and clipping efficiency were measured simultaneously and we were able to measure K_D in the absence of clipping.

X-ToF Sensor for Determining Salt Effects on k_{clip} of Xrn1

To monitor the catalytic action of Xrn1 at the single-nucleotide level, the dToF reader was employed to detect and identify rNMPs in real-time. Following the association of a single RNA molecule to Xrn1 within the INER, the Mg^{2+} cofactor was electrokinetically introduced by applying a voltage between the accessory and ToF channel while the input−output channels remained floating. As shown in Figure 6A(i), increasing the applied voltage enhanced fluid velocity facilitating the transport of cofactor into the reaction zone and rNMPs into the flight tube. Upon contact with Mg^{2+}, Xrn1 initiated its processive clipping of Cas9 RNA releasing individual rNMPs sequentially.

The released rNMPs were electrokinetically transported through the dToF reader. The ToF is determined by the apparent electrophoretic mobility of the molecule and its characteristic interactions with the flight tube walls.[4,7,14] The dToF reader was engineered to provide a significant voltage drop (65%) within the flight tube while maintaining detectable RPS signals via a 20% voltage drop across the pores.[14] Each rNMP is represented by "paired events" in the RPS current trace; thus, the total number of clipped rNMPs is directly identified by counting these paired events. By correlating the total event count with the time required for full digestion, the clipping rate (k_{clip}) could be calculated as detailed in Figure 6A(ii).

Control experiments lacking either the cofactor or the RNA substrate showed an absence of RPS events (Figure 6B(i,ii)). In contrast, the addition of Mg^{2+} to the Xrn1/RNA complex yielded discernible signals with a significantly higher event frequency observed at lower KCl concentrations (Figure 6B(iii,iv)). In 100 mM KCl, the dToF reader registered 8750 events indicating that Xrn1 successfully digested the entire Cas9 RNA strand, which is consistent with our IMER results.[11] Under these optimal conditions, we found that k_{clip} for immobilized Xrn1 in the INER was 23 ± 15 nt s^{-1}. However, in the case of 1 M KCl, k_{clip} decreased to 9 nt s^{-1}.

We also implemented a secondary method to verify k_{clip} by analyzing the temporal spacing between individual event pairs in the RPS trace. As seen in Figure 6D(i), the interval between event pairs represents the discrete time required for the enzyme to clip a single rNMP. Averaging these intervals across the entire RPS trace yielded a k_{clip} of 23 ± 5 nt s^{-1}(Figure 6D(ii)), aligning closely with our previous results. The amplitude difference between the paired peaks (Figure 6D(i)) arises from minor geometric pore asymmetries and local ion concentration polarization (ICP). Because the permselective nanopores drive unequal ion transport under an applied voltage, localized salt gradients (enrichment and depletion zones) form within the nanoflight tube. This altered local conductivity shifts the baseline current and blockade amplitude for each pore, as corroborated by our COMSOL simulations (see Supporting Information).

The salt-dependent modulation of enzyme activity likely arises from several factors including neutralization of electrostatic interactions and alterations in overall enzyme stability. For Xrn1, aspartic and glutamic acid residues in the active site coordinate two Mg^{2+} ions to bind the RNA phosphate group and induce hydrolysis. Excess counterions can screen these Mg^{2+} ions, hindering the enzyme's ability to move along the RNA backbone. Notably, because the enzymes are anchored to the INER surface, their motor activity remains largely unimpeded; Xrn1 successfully digested the ∼1.2 μm contour length of the Cas9 RN, demonstrating robust processivity in the nanofluidic environment.

CONCLUSION

The X-ToF sensor provides an innovative platform for single-molecule sensing by integrating single molecule enzymatic reactions with the ability to monitor their reaction products in real time. Conventional membrane-suspended nanopores, on the other hand, typically use bulk biological reactions off-chip with products loaded into the nanopore sensor following the enzymatic reaction; single enzyme reactions are not monitored. Another critical innovation of this work was the use of engineered surfaces made possible using plastics and proper

https://doi.org/10.1021/acsami.6c08660
ACS Appl. Mater. Interfaces 2026, 18, 38600−38614

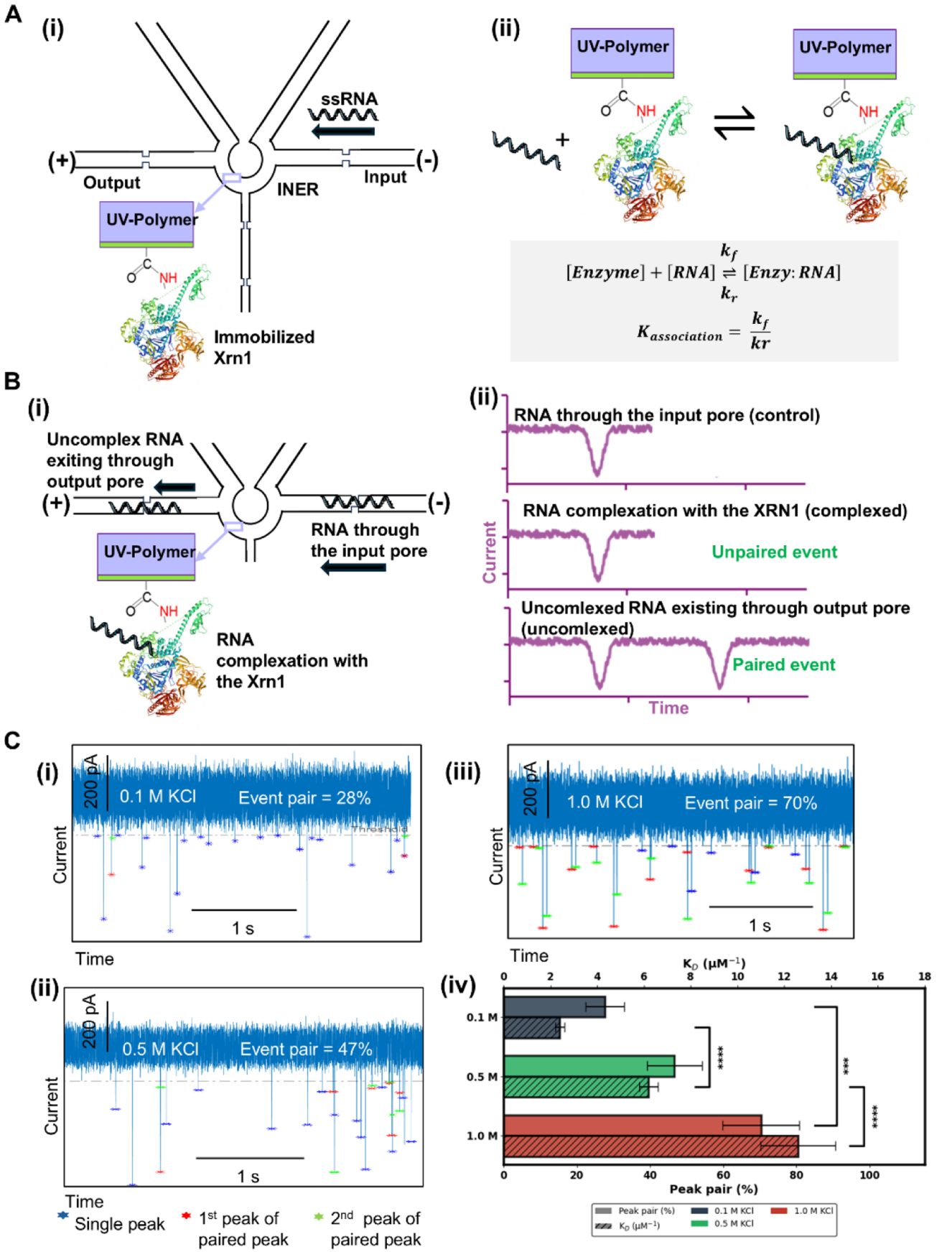

Figure 5. Measuring the association thermodynamics between Xrn1 and Cas9 RNA at the single-molecule level. (A) Schematic of the single-molecule measurement process: (i) RNA migrating against EOF within the INER and through the input nanopore; (ii) thermodynamic parameters obtained during the loading step. (B) (i) In-plane pores flanking the INER distinguish between association (single event) and no association

https://doi.org/10.1021/acsami.6c08660
ACS Appl. Mater. Interfaces 2026, 18, 38600−38614

Figure 5. continued

(paired events); (ii) illustration of the three RPS response types based on enzyme interaction with its migrating RNA substrate. (C) (i−iii) RPS traces for 0.1, 0.5, and 1.0 M KCl; (iv) chart showing percentages of paired events and K_D values for each concentration. Conditions: 10 pg RNA mass load at loading voltage of 0.5 V.

UV/O_3 dosing, which allowed reconciliation between the disparate salt requirements of bioenzyme activity and RPS.

The operation of the X-ToF sensor that uses a two-step process (loading step of the substrate followed by clipping step) can deduce the complex dynamics of processive enzymes that were successfully evaluated using a single molecule reaction. Compared to current gold-standard techniques like single-molecule FRET, which require complex fluorescent labeling, which can alter enzyme behavior, the X-ToF achieves this kinetic profiling completely label-free. Furthermore, while optical methods often struggle to decouple the association from the cleavage phase, our platform offers distinct spatial and temporal resolution to discretely monitor both binding and processive clipping independently.

Beyond studying the complex dynamics of processive exonucleases like Xrn1, the X-ToF sensor holds potential for diverse applications, including DNA/RNA and protein sequencing. Repurposing the device for different sequencing modalities requires only a change of the immobilized enzyme within the INER. Furthermore, the dual-parameter readout (RPS and ToF) provides high multiplexing power necessary to identify epigenetic, epitranscriptomic, or post-translational modifications.[13] Given that over 170 post-transcriptional RNA modifications exist, the X-ToF sensor addresses a need in molecular biology by providing a tool capable of resolving these complex signatures at the single-molecule level. However, for this to be possible, the dToF reader of X-ToF must be able to efficiently differentiate between subtle molecular changes between the individual ribonucleotides in the case of RNA sequencing. Preliminary data indicating this capability are shown in Figure S7 in which the rNMPs were successfully identified using the dToF and the molecular-dependent ToF for each nucleotide.

EXPERIMENTAL SECTION

Reagents and Materials

Cyclic olefin copolymer (COC 8007, Tg = 78 °C, thickness 100 μm) cover plates were purchased from TOPAS Advanced Polymers (Florence, KY). Cyclic olefin polymer (COP 1060R, Tg = 100 °C) substrates were obtained from Knightsbridge Plastics Inc. (CA, USA). Polyurethane acrylate (PUA) MINS-511RM resin was purchased from Chang Sung Sheet, Ltd. (Gyeonggi-do, South Korea). Poly(methyl methacrylate) (PMMA, Tg = 105 °C) was obtained from ePlastics (San Diego, CA). Ribonucleotide monophosphates (rNMPs) and polyethylene terephthalate (PET) were purchased from Sigma-Aldrich. Lambda DNA (48,502 bp), λ-exonuclease (λ-Exo), ThermoPol, CutSmart buffers, Xrn1, and 10× NEBuffer were obtained from New England Biolabs (Ipswich, MA). High Sensitivity D1000 ScreenTape, D1000 Sample Buffer, and D1000 Ladder, as well as High Sensitivity RNA ScreenTape, RNA Sample Buffer, and RNA Ladder, were purchased from Agilent Technologies (Santa Clara, CA). A 60 nt RNA was obtained from Integrated DNA Technologies, Inc. (Skokie, IL), and Cas9 RNA was purchased from TriLink BioTechnologies (San Diego, CA).

METHODS

AFM Images

The AFM used was purchased from Shimadzu, Corp. (SPM HT-9700). The probe used for imaging was a Super Sharp Silicon tip (Nanosensors, Switzerland) with a tip radius <2 nm, half cone angle of 10°, aspect ratio 4:1 at 200 nm from the tip apex, and a frequency of 300 kHz. A dynamic scanning mode was used for imaging with a scanning frequency of 0.5 Hz. The acquired images were analyzed using SPM Manager v4.76.1 software.

Surface Activation of Thermoplastics

Thermoplastic surfaces were activated with UV/O_3 generated by a low-pressure Hg lamp (Jelight, CA). Samples were placed 1 cm from the light source (intensity: 20 mW cm^{-2}) for 0−15 min (0, 0.5, 1.5, 3.5, 5.5, 10, or 15 min). Lamp output at 254 nm was measured prior to activation to ensure reproducibility.

Water Contact Angle Measurements

Water contact angles (WCAs) were measured using a VCA Optima instrument. Two μL of nanopure water (pH 7.5) were deposited on COP surfaces, and WCAs were recorded with the manufacturer's software. Reported values are the mean of nine replicates from different substrate positions.

Device Fabrication

Device fabrication[5] is described in Supporting Information and Figure S2.

Scanning Electron Microscopy

Devices were sputter-coated with a 2 nm Ir layer using an EMS 150ES coater. SEM imaging was performed with a Hitachi SU8230 FE-SEM at 1 kV (intermediate resin stamp) and 5 kV (thermoplastic substrates), with a working distance of 7.9−9.9 mm. Images were analyzed using ImageJ and Fiji software.

Ag/AgCl Electrodes

Standard electrical wires were soldered to 1.5 cm silver wires (0.25 mm dia., 99.9%) and connector pins. Both joints were insulated with rubber covers. The silver wires were chlorinated by immersion in 99% household bleach for 15 min to form Ag/AgCl.

COMSOL Simulations

Finite element modeling was performed using COMSOL Multiphysics v5.5 prior (see Supporting Information Figure S9 and Tables S1 and S2).

λ-Exo Purification and Immobilization

λ-Exo was concentrated using a 10 kDa MWCO Amicon Ultra centrifugal filter (Millipore Sigma). Four mL enzyme solution was centrifuged at 4000*g* for 80 min at room temperature, and the concentrate was collected. Immobilization onto IMER devices was performed using EDC/NHS coupling.[11] Devices were filled with 20 mg EDC and 2 mg NHS in 0.1 M MES buffer (pH 4.8) and incubated for 30 min. After hydrodynamic displacement, λ-Exo (0.35 μg/μL) was introduced and incubated for 24 h at 4 °C. Devices were rinsed with 1× reaction buffer to remove unbound enzyme.

Digestion of DNA

In Solution. 50 μL reactions containing 10 μL λ-DNA or Cas9 RNA (0.1 μg/μL), 5 μL 10× reaction buffer, 1 μL λ-Exo or Xrn1, and 34 μL nuclease-free water were incubated at 37 °C for 30 min. Reactions were stopped with 10 mM EDTA and heat-inactivated at 75 °C for 10 min.

https://doi.org/10.1021/acsami.6c08660
ACS Appl. Mater. Interfaces 2026, 18, 38600−38614

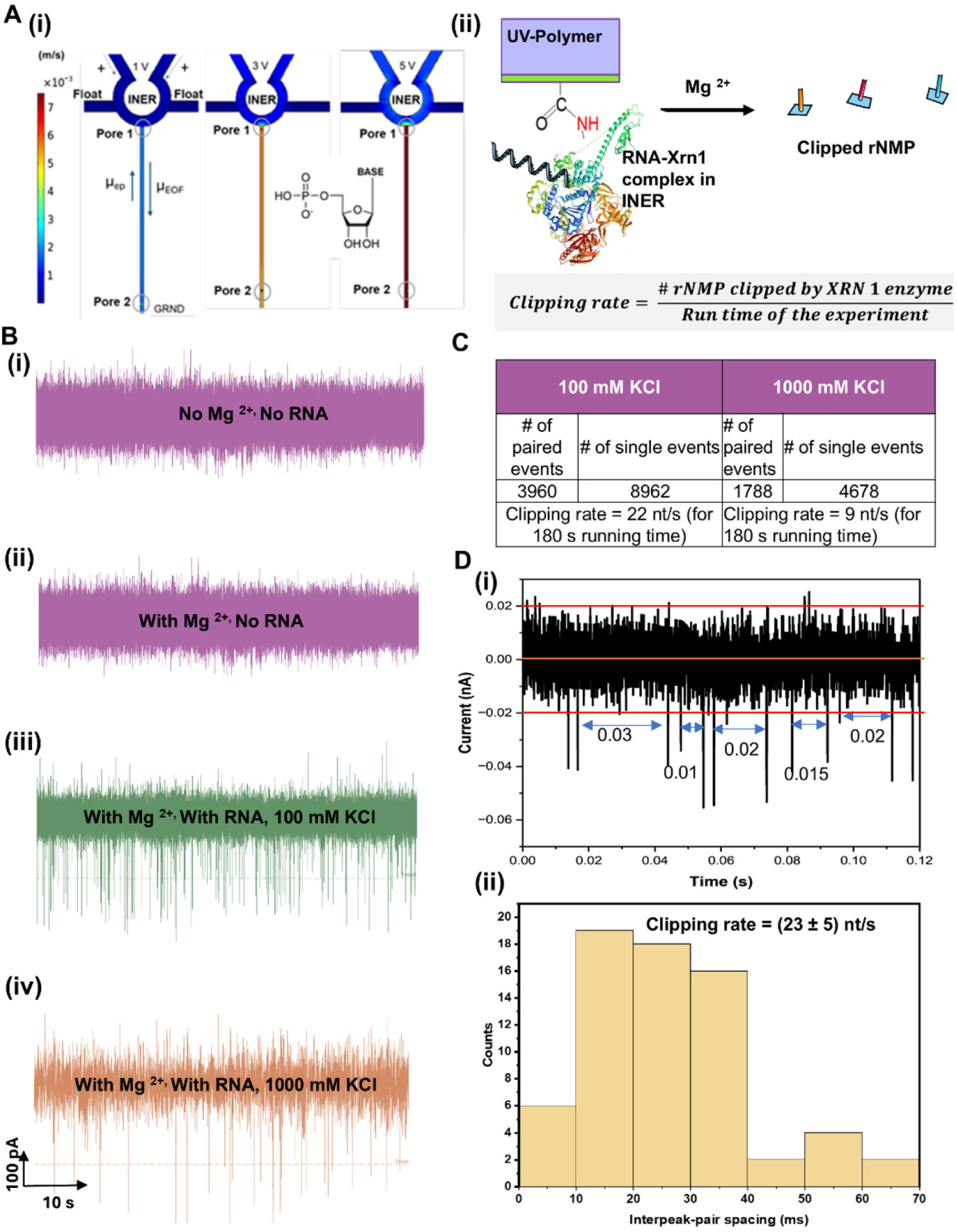

Figure 6. Real-time monitoring of the Xrn1 processive of Cas9 RNA cleavage. (A) (i) COMSOL simulation showing the voltage distribution of the INER through the dToF reader; (ii) schematic showing Mg^{2+} dependent RNA digestion and k_{clip}-dependent arrival rate of rNMPs into the dToF reader. (B) RPS current traces for (i,ii) negative controls and digestions at (iii) 100 mM and (iv) 1000 mM KCl. (C) Table summarizing Xrn1 clipping rates (k_{clip}) at low and high salt concentrations. (D) Analysis of k_{clip} via interevent spacing: (i) Representative RPS trace data where the

https://doi.org/10.1021/acsami.6c08660
ACS Appl. Mater. Interfaces 2026, 18, 38600−38614

Figure 6. continued

time interval between paired events corresponds to the enzymatic turnover time of a single rNMP; (ii) histogram of interevent times used to calculate the average k_{clip} as the inverse of the mean interval.

Solid Phase. λ-DNA was pumped through immobilized devices at 0.5 μL/min using a syringe pump. Six μL effluent fractions were collected every 12 min and analyzed with the TapeStation. For RNA digestions, 50 μL reactions contained 2 μL Cas9 RNA (10 ng/μL), 5 μL 10× reaction buffer, 2 μL Xrn1, and 41 μL nuclease-free water. Reactions were incubated for 60 s at room temperature, quenched with 4 μL 500 mM EDTA, and desalted using Zeba spin columns before TapeStation analysis.

TapeStation Analysis

RNA and DNA digestion products were analyzed on the Agilent TapeStation using the manufacturer's High Sensitivity RNA ScreenTape and D1000 ScreenTape Quick Guides.

Enzyme Immobilization – Xrn1 to INER

Xrn1 immobilization was performed using EDC/NHS chemistry. After UV/O_3 activation, COC and COP substrates were bonded with HEX03. Channels were filled with NEBuffer 3 (100 mM NaCl, 50 mM Tris–HCl, 1 mM DTT, pH 7.9). INER microchannels were replaced with 0.1 M MES buffer containing 10 mg EDC and 1 mg NHS, and a 5 V bias was applied for 30 min. The solution was then replaced with 737 nM Xrn1, which was driven through the INER at 5 V for 30 min followed by a 90 min incubation.

Site-Specific Immobilization Validation

Devices were primed with 50% MeOH (5 min) and PBS (15 min). A solution of 50 nM Cy3-labeled oligonucleotide and 20 mg/mL EDC in PBS was introduced,[11] followed by 5 V bias for 15 min. The solution was removed under vacuum, washed with 0.05% Tween-20 and 50% MeOH, and imaged by epifluorescence microscopy (λ_{ex} = 532 nm). Controls without EDC confirmed negligible nonspecific adsorption.

Loading Single Molecules into X-ToF Sensor

X-ToF devices were filled with buffer (100 mM NaCl, 50 mM Tris–HCl, 1 mM DTT, pH 7.9). SYTO82-labeled Cas9 RNA (4521 nt) was introduced via the input funnel. Electrodes connected to a waveform generator were placed in reservoirs flanking the INER. The device was mounted on an epifluorescence microscope (100×/1.4 NA objective) with an EMCCD camera. Excitation was provided by a 532 nm Nd/YAG laser (0.01–5 W).[9,23] Cas9 RNA was electrokinetically driven at 1–2 V DC, and images were collected. Fluorescence intensity was processed in Origin using a 50% percentile filter. The same procedure was applied to POPO-stained DNA.

Cas9–Xrn1 Digestion

SYTO82-labeled Cas9 RNA containing 4% β-mercaptoethanol was introduced into X-ToF devices filled with NEBuffer 3 lacking Mg^{2+}. RNA was directed to the INER, and fluorescence was monitored after voltage removal. The experiment was repeated with NEBuffer 3 containing 10 mM $MgCl_2$. Fluorescence decay was used to calculate clipping rates.

Determination of K_D for Xrn1–Cas9 RNA

Input/output channels of Xrn1-immobilized sensors were filled with NEBuffer containing KCl (0.1, 0.5, or 1.0 M). Buffer blanks were recorded before Cas9 RNA was introduced under the same conditions. Current traces were recorded, and K_D was calculated from the ratio of peak pairs (unbound Cas9) to single peaks (Cas9–Xrn1 complexes).

Identification of Xrn1 Digested Products and Determination of k_{clip}

To ensure single-molecule delivery, Cas9 RNA (10 pM) was introduced using a carefully controlled applied voltage (2 V). Once the first blockade signal at the input pore was detected confirming that a single RNA molecule had entered and been successfully isolated the voltage supply was disconnected. Following this capture confirmation, the Mg^{2+} cofactor was manually introduced into the accessory channel. Finally, an applied voltage (4 V) from the accessory channel to the sensing channel was initiated to drive the Mg^{2+} to the immobilized enzyme and commence RNA digestion. k_{clip} was calculated from the number of events within 180 s.

rNMP Translocation

Solutions of rNMPs (1 nM each) were prepared in NEBuffer 3 (pH 7.8) with 0.1 M KCl. Devices were filled, connected to a TIA via Ag/AgCl electrodes, and a 4 V bias was applied. Linear I–V curves confirmed device function. After equilibrium, blank traces were recorded, followed by dNMP measurements. Signals were amplified with a TIA (100 nA/V) with a 10 kHz low-pass filter, digitized at 250 kHz (NI USB-6343 DAQ), and recorded in LabVIEW. Postprocessing included 100 Hz high-pass filtering for baseline correction and 10 kHz third-order low-pass filtering.

RPS Data Analysis

RPS data were analyzed in MATLAB R2022b using custom software (EventFinder v.269). Translocation events were defined as resistive pulses with amplitudes ≥ 5σ of baseline RMS noise. Peak amplitude (ΔI), dwell time (fwhm), and ToFs were extracted from filtered traces. Event pairing for ToF followed modified protocols from previous dNMP and dye-labeled rNMP studies.[7,14] Log-transformed ToFs were Gaussian-fitted, and correlated pairs within ±3σ of the mean were retained. ΔI and dwell time were averaged across pores, with ΔI normalized to baseline current (ΔI/Io) for plotting box plt and histograms. Data was exported to Excel, and PCA and K-means clustering were performed in Google Colab (data not shown) (SciPy, NumPy, Matplotlib, Pandas, Seaborn, Scikit-learn).

■ ASSOCIATED CONTENT

Supporting Information

The Supporting Information is available free of charge at https://pubs.acs.org/doi/10.1021/acsami.6c08660.

Fabrication method of X-ToF; X-ToF equivalent circuits; salt effects on exonucleases; surface engineering to mitigate salt effects; surface distribution of –COOH groups; Xrn1 structure; salt effects on RPS; ToF measurements on rNMPs (PDF)

■ AUTHOR INFORMATION

Corresponding Authors

Adam R. Hall – *Center of Biomodular Multiscale Systems for Precision Medicine, The University of Kansas, Lawrence, Kansas 66045, United States; Virginia Tech-Wake Forest School of Biomedical Engineering and Sciences, Wake Forest School of Medicine, Winston Salem, North Carolina 27101, United States*; Email: adam.hall@wfusm.edu

Sunggook Park – *Center of Biomodular Multiscale Systems for Precision Medicine, The University of Kansas, Lawrence, Kansas 66045, United States; Department of Industrial & Mechanical Engineering, Louisiana State University, Baton Rouge, Louisiana 70803, United States*; orcid.org/0000-0003-0424-6318; Email: sunggook@lsu.edu

Steven A. Soper – *Department of Chemistry, The University of Kansas, Lawrence, Kansas 66045, United States; Center of Biomodular Multiscale Systems for Precision Medicine, Bioengineering Program, and Department of Mechanical*

Engineering, The University of Kansas, Lawrence, Kansas 66045, United States; KU Cancer Center, University of Kansas Medical Center, Kansas City, Kansas 66160, United States; orcid.org/0000-0002-8292-7058; Email: ssoper@ku.edu

Authors

Indu A. Chandrasoma – *Department of Chemistry, The University of Kansas, Lawrence, Kansas 66045, United States; Center of Biomodular Multiscale Systems for Precision Medicine, The University of Kansas, Lawrence, Kansas 66045, United States*

Khurshed Akabirov – *Department of Chemistry, The University of Kansas, Lawrence, Kansas 66045, United States; Center of Biomodular Multiscale Systems for Precision Medicine, The University of Kansas, Lawrence, Kansas 66045, United States*

Oluwadamilola Fateru – *Department of Chemistry, The University of Kansas, Lawrence, Kansas 66045, United States; Center of Biomodular Multiscale Systems for Precision Medicine, The University of Kansas, Lawrence, Kansas 66045, United States*

Katie Childers – *Center of Biomodular Multiscale Systems for Precision Medicine and Bioengineering Program, The University of Kansas, Lawrence, Kansas 66045, United States*

Swarnagowri Vaidyanathan – *Department of Chemistry, The University of Kansas, Lawrence, Kansas 66045, United States; Center of Biomodular Multiscale Systems for Precision Medicine, The University of Kansas, Lawrence, Kansas 66045, United States*

Sheila M. Barros – *Department of Chemistry, The University of Kansas, Lawrence, Kansas 66045, United States; Center of Biomodular Multiscale Systems for Precision Medicine, The University of Kansas, Lawrence, Kansas 66045, United States;* orcid.org/0000-0003-3332-299X

Maximillian Chibuike – *Department of Chemistry, The University of Kansas, Lawrence, Kansas 66045, United States; Center of Biomodular Multiscale Systems for Precision Medicine, The University of Kansas, Lawrence, Kansas 66045, United States*

Suresh Shivanka – *Department of Chemistry, The University of Kansas, Lawrence, Kansas 66045, United States; Center of Biomodular Multiscale Systems for Precision Medicine, The University of Kansas, Lawrence, Kansas 66045, United States*

Matthew Verber – *Center of Biomodular Multiscale Systems for Precision Medicine, The University of Kansas, Lawrence, Kansas 66045, United States; Department of Chemistry, University of North Carolina, Chapel Hill, Chapel Hill, North Carolina 27599, United States*

Collin McKinney – *Center of Biomodular Multiscale Systems for Precision Medicine, The University of Kansas, Lawrence, Kansas 66045, United States; Department of Chemistry, University of North Carolina, Chapel Hill, Chapel Hill, North Carolina 27599, United States*

Uditha Athapattu – *Department of Chemistry, The University of Kansas, Lawrence, Kansas 66045, United States; Center of Biomodular Multiscale Systems for Precision Medicine, The University of Kansas, Lawrence, Kansas 66045, United States*

Pubudu Premarathne – *Department of Chemistry, The University of Kansas, Lawrence, Kansas 66045, United States; Center of Biomodular Multiscale Systems for Precision Medicine, The University of Kansas, Lawrence, Kansas 66045, United States*

Farhad Shiri – *Department of Chemistry, The University of Kansas, Lawrence, Kansas 66045, United States; Center of Biomodular Multiscale Systems for Precision Medicine, The University of Kansas, Lawrence, Kansas 66045, United States*

Malgorzata A. Witek – *Department of Chemistry, The University of Kansas, Lawrence, Kansas 66045, United States; Center of Biomodular Multiscale Systems for Precision Medicine, The University of Kansas, Lawrence, Kansas 66045, United States*

Junseo Choi – *Center of Biomodular Multiscale Systems for Precision Medicine, The University of Kansas, Lawrence, Kansas 66045, United States; Department of Engineering Technology, Texas State University, San Marcos, Texas 78666, United States;* orcid.org/0000-0002-3461-3820

Complete contact information is available at: https://pubs.acs.org/10.1021/acsami.6c08660

Notes

The authors declare no competing financial interest.

■ ACKNOWLEDGMENTS

The authors thank the NIH for financial support of this work via the NIH/NIBIB funded Center of BioModular Multiscale Systems for Precision Medicine (P41-EB020594, R01-EB031579; R33-CA235597, R21-CA277351; P20-GM130423; and P20-GM103638).

■ REFERENCES

(1) (a) Butler, T. Z.; Pavlenok, M.; Derrington, I. M.; Niederweis, M.; Gundlach, J. H. Single-molecule DNA detection with an engineered MspA protein nanopore. *Proc. Natl. Acad. Sci. U. S. A.* **2008**, *105* (52), 20647–20652. (b) Nivala, J.; Marks, D. B.; Akeson, M. Unfoldase-mediated protein translocation through an α-hemolysin nanopore. *Nat. Biotechnol.* **2013**, *31* (3), 247–250.

(2) (a) Xia, Z.; Scott, A.; Keneipp, R.; Chen, J.; Niedzwiecki, D. J.; DiPaolo, B.; Drndic, M. Silicon Nitride Nanopores Formed by Simple Chemical Etching: DNA Translocations and TEM Imaging. *ACS Nano* **2022**, *16* (11), 18648–18657. (b) Smeets, R.; Kowalczyk, S. W.; Hall, A.; Dekker, N.; Dekker, C. Translocation of RecA-coated double-stranded DNA through solid-state nanopores. *Nano Lett.* **2009**, *9* (9), 3089–3095.

(3) Kowalczyk, S. W.; Tuijtel, M. W.; Donkers, S. P.; Dekker, C. Unraveling single-stranded DNA in a solid-state nanopore. *Nano Lett.* **2010**, *10* (4), 1414–1420.

(4) Athapattu, U. S.; Rathnayaka, C.; Vaidyanathan, S.; Gamage, S. S.; Choi, J.; Riahipour, R.; Manoharan, A.; Hall, A. R.; Park, S.; Soper, S. A. Tailoring thermoplastic in-plane nanopore size by thermal fusion bonding for the analysis of single molecules. *ACS Sens.* **2021**, *6* (8), 3133–3143.

(5) Shiri, F.; Choi, J.; Vietz, C.; Rathnayaka, C.; Manoharan, A.; Shivanka, S.; Li, G.; Yu, C.; Murphy, M. C.; Soper, S. A.; et al. Nano-injection molding with resin mold inserts for prototyping of nanofluidic devices for single molecular detection. *Lab Chip* **2023**, *23* (22), 4876–4887.

(6) (a) Shivanka, S.; Shiri, F.; Chibuike, M.; McKinney, C.; Verber, M.; Choi, J.; Park, S.; Hall, A. R.; Soper, S. A. Insights on using plastic-based dual in-plane nanopore sensors for differentiation and shape determinations of single protein molecules. *Sci. Rep.* **2025**, *15*, 13742. (b) Chibuike, M.; Rathnayaka, C.; Shivanka, S.; Choi, J.; Verber, M.; Park, S.; Soper, S. A. Millisecond Label-Free Single Peptide Detection and Identification Using Nanoscale Electrochromatography and Resistive Pulse Sensing. *Anal. Chem.* **2024**, *97*, 427–435.

(7) Choi, J.; Jia, Z.; Riahipour, R.; McKinney, C. J.; Amarasekara, C. A.; Weerakoon-Ratnayake, K. M.; Soper, S. A.; Park, S. Label-Free

Identification of Single Mononucleotides by Nanoscale Electrophoresis. *Small* **2021**, *17* (42), No. e2102567.
(8) Uba, F. I.; Hu, B.; Weerakoon-Ratnayake, K.; Oliver-Calixte, N.; Soper, S. A. High process yield rates of thermoplastic nanofluidic devices using a hybrid thermal assembly technique. *Lab Chip* **2015**, *15* (4), 1038−1049.
(9) O'Neil, C.; Amarasekara, C. A.; Weerakoon-Ratnayake, K. M.; Gross, B.; Jia, Z.; Singh, V.; Park, S.; Soper, S. A. Electrokinetic transport properties of deoxynucleotide monophosphates (dNMPs) through thermoplastic nanochannels. *Anal. Chim. Acta* **2018**, *1027*, 67−75.
(10) ONeil, C. E.; Jackson, J. M.; Shim, S.-H.; Soper, S. A. Interrogating surface functional group heterogeneity of activated thermoplastics using super-resolution fluorescence microscopy. *Anal. Chem.* **2016**, *88* (7), 3686−3696.
(11) Athapattu, U. S.; Amarasekara, C. A.; Immel, J. R.; Bloom, S.; Barany, F.; Nagel, A. C.; Soper, S. A. Solid-phase XRN1 reactions for RNA cleavage: application in single-molecule sequencing. *Nucleic Acids Res.* **2021**, *49* (7), No. e41.
(12) Nagarajan, V. K.; Jones, C. I.; Newbury, S. F.; Green, P. J. XRN 5′→ 3′ exoribonucleases: structure, mechanisms and functions. *Biochim. Biophys. Acta, Gene Regul. Mech.* **2013**, *1829* (6−7), 590−603.
(13) Shiri, F.; Choi, J.; Vietz, C.; Rathnayaka, C.; Manoharan, A.; Shivanka, S.; Li, G.; Yu, C.; Murphy, M. C.; Soper, S. A.; et al. Nano-injection molding with resin mold inserts for prototyping of nanofluidic devices for single molecular detection. *Lab Chip* **2023**, *23* (22), 4876−4887.
(14) Rathnayaka, C.; Chandrosoma, I. A.; Choi, J.; Childers, K.; Chibuike, M.; Akabirov, K.; Shiri, F.; Hall, A. R.; Lee, M.; McKinney, C.; et al. Detection and identification of single ribonucleotide monophosphates using a dual in-plane nanopore sensor made in a thermoplastic via replication. *Lab Chip* **2024**, *24* (10), 2721−2735.
(15) Oliver-Calixte, N. J.; Uba, F. I.; Battle, K. N.; Weerakoon-Ratnayake, K. M.; Soper, S. A. Immobilization of lambda exonuclease onto polymer micropillar arrays for the solid-phase digestion of dsDNAs. *Anal. Chem.* **2014**, *86* (9), 4447−4454.
(16) Lepoitevin, M.; Coulon, P. E.; Bechelany, M.; Cambedouzou, J.; Janot, J.-M.; Balme, S. Influence of nanopore surface charge and magnesium ion on polyadenosine translocation. *Nanotechnology* **2015**, *26* (14), 144001.
(17) Diederichs, T.; Pugh, G.; Dorey, A.; Xing, Y.; Burns, J. R.; Hung Nguyen, Q.; Tornow, M.; Tampé, R.; Howorka, S. Synthetic protein-conductive membrane nanopores built with DNA. *Nat. Commun.* **2019**, *10* (1), 5018.
(18) Uba, F. I.; Pullagurla, S. R.; Sirasunthorn, N.; Wu, J.; Park, S.; Chantiwas, R.; Cho, Y.-K.; Shin, H.; Soper, S. A. Surface charge, electroosmotic flow and DNA extension in chemically modified thermoplastic nanoslits and nanochannels. *Analyst* **2015**, *140* (1), 113−126.
(19) (a) Smeets, R. M.; Keyser, U. F.; Krapf, D.; Wu, M.-Y.; Dekker, N. H.; Dekker, C. Salt dependence of ion transport and DNA translocation through solid-state nanopores. *Nano Lett.* **2006**, *6* (1), 89−95. (b) Wadsworth, I. D.; Hall, A. R. Effects of symmetric and asymmetric salt conditions on a selective solid-state nanopore assay. *Nano Res.* **2022**, *15* (11), 9936−9942. (c) Wanunu, M.; Morrison, W.; Rabin, Y.; Grosberg, A. Y.; Meller, A. Electrostatic focusing of unlabelled DNA into nanoscale pores using a salt gradient. *Nat. Nanotechnol.* **2010**, *5*, 160−165.
(20) Longley, M.; Mosbaugh, D. Properties of the 3 'to 5 'exonuclease associated with porcine liver DNA polymerase gamma. Substrate specificity, product analysis, inhibition, and kinetics of terminal excision. *J. Biol. Chem.* **1991**, *266* (36), 24702−24711.
(21) (a) Park, C.; Raines, R. T. Quantitative analysis of the effect of salt concentration on enzymatic catalysis. *J. Am. Chem. Soc.* **2001**, *123* (46), 11472−11479. (b) Warren, J. C.; Stowring, L.; Morales, M. F. The effect of structure-disrupting ions on the activity of myosin and other enzymes. *J. Biol. Chem.* **1966**, *241* (2), 309−316.
(22) Bauduin, P.; Nohmie, F.; Touraud, D.; Neueder, R.; Kunz, W.; Ninham, B. W. Hofmeister specific-ion effects on enzyme activity and buffer pH: Horseradish peroxidase in citrate buffer. *J. Mol. Liq.* **2006**, *123* (1), 14−19.
(23) Amarasekara, C. A.; Rathnayaka, C.; Athapattu, U. S.; Zhang, L.; Choi, J.; Park, S.; Nagel, A. C.; Soper, S. A. Electrokinetic identification of ribonucleotide monophosphates (rNMPs) using thermoplastic nanochannels. *J. Chromatogr. A* **2021**, *1638*, 461892.

https://doi.org/10.1021/acsami.6c08660
ACS Appl. Mater. Interfaces 2026, 18, 38600−38614